AGU PUBLICATIONS

JGR

Journal of Geophysical Research: Atmospheres

RESEARCH ARTICLE
10.1002/2015JD024261

Special Section:
East Asian Study of Tropospheric Aerosols and Impact on Cloud and Precipitation

Aerosol characterization over the North China Plain: Haze life cycle and biomass burning impacts in summer

Yele Sun[1,2], Qi Jiang[1], Yisheng Xu[3], Yan Ma[4], Yingjie Zhang[1,5], Xingang Liu[6], Weijun Li[7], Fei Wang[3], Jie Li[1], Pucai Wang[8], and Zhanqing Li[9]

[1]State Key Laboratory of Atmospheric Boundary Layer Physics and Atmospheric Chemistry, Institute of Atmospheric Physics, Chinese Academy of Sciences, Beijing, China, [2]Center for Excellence in Urban Atmospheric Environment, Institute of Urban Environment, Chinese Academy of Sciences, Xiamen, China, [3]Chinese Research Academy of Environmental Sciences, Beijing, China, [4]Jiangsu Key Laboratory of Atmospheric Environment Monitoring and Pollution Control, Nanjing University of Information Science and Technology, Nanjing, China, [5]School of Atmospheric Physics, Nanjing University of Information Science and Technology, Nanjing, China, [6]State Key Laboratory of Water Environment Simulation, School of Environment, Beijing Normal University, Beijing, China, [7]Environment Research Institute, Shandong University, Jinan, China, [8]Key Laboratory of Middle Atmosphere and Global Environment Observation, Institute of Atmospheric Physics, Chinese Academy of Sciences, Beijing, China, [9]College of Global Change and Earth System Science, Beijing Normal University, Beijing, China

Abstract The North China Plain experiences frequent severe haze pollution during all seasons. Here we present the results from a summer campaign that was conducted at Xianghe, a suburban site located between the megacities of Beijing and Tianjin. Aerosol particle composition was measured in situ by an Aerosol Chemical Speciation Monitor along with a suite of collocated measurements during 1–30 June 2013. Our results showed that aerosol composition at the suburban site was overall similar to that observed in Beijing, which was mainly composed of organics (39%), nitrate (20%), and sulfate (18%). Positive matrix factorization of organic aerosol (OA) identified four OA factors with different sources and processes. While secondary organic aerosol dominated OA, on average accounting for 70%, biomass burning OA (BBOA) was also observed to have a considerable contribution (11%) for the entire study period. The contribution of BBOA was increased to 21% during the BB period in late June, indicating a large impact of agricultural burning on air pollution in summer. Biomass burning also exerted a significant impact on aerosol optical properties. It was estimated that ~60% enhancement of absorption at the ultraviolet spectral region was caused by the organic compounds from biomass burning. The formation mechanisms and sources of severe haze pollution episodes were investigated in a case study. The results highlighted two different mechanisms, i.e., regional transport and local sources, driving the haze life cycles differently in summer in the North China Plain. While secondary aerosol species dominated aerosol composition in the episode from regional transport, organics and black carbon comprised the major fraction in the locally formed haze episode.

Key Points:
- Similar aerosol composition between a suburban site in North China and the megacity of Beijing
- Significant impacts of biomass burning on aerosol composition and absorption coefficients
- Two different mechanisms, i.e., regional transport and local sources driving haze life cycles

Supporting Information:
- Supporting Information S1

Correspondence to:
Y. Sun,
sunyele@mail.iap.ac.cn

Citation:
Sun, Y., et al. (2016), Aerosol characterization over the North China Plain: Haze life cycle and biomass burning impacts in summer, *J. Geophys. Res. Atmos.*, *121*, 2508–2521, doi:10.1002/2015JD024261.

Received 22 SEP 2015
Accepted 24 FEB 2016
Accepted article online 29 FEB 2016
Published online 14 MAR 2016

1. Introduction

Haze episodes frequently occur in the North China Plain [*Liu et al.*, 2013; *Sun et al.*, 2013b, 2014; *Yang et al.*, 2015; *Zhao et al.*, 2013], not only causing severe air pollution but also exerting harmful effects on human health [*Cao et al.*, 2012; *S. Zheng et al.*, 2015]. The formation of haze episodes particularly during wintertime is rapid, often within a few hours. Such a rapid formation of haze was found to be mainly driven by the changes of meteorological conditions associated with enhanced secondary aerosol formation and regional transport [*Sun et al.*, 2014; *G. J. Zheng et al.*, 2015]. Source apportionment analyses also revealed the importance of primary sources including residential coal combustion, traffic emissions, and cooking activities [*Huang et al.*, 2014; *Sun et al.*, 2014]. These results together suggest that the formation of severe haze pollution is a combined result of stagnant meteorology, primary emissions, and secondary aerosol formation. However, most previous studies on the sources and evolution processes of severe haze pollution were conducted in winter, a season with the most frequent occurrence of haze and in megacities [*Chen et al.*, 2015; *Jiang et al.*, 2015; *Liu et al.*, 2013; *Sun et al.*, 2006, 2013b, 2014; *Yang et al.*, 2015; *J. K. Zhang et al.*, 2014; *Zhao et al.*, 2013]; the haze life cycle during other seasons at the suburban sites in the North China Plain remain poorly understood.

Biomass burning is a large contributor to particulate matter (PM) pollution during harvest seasons [*Cheng et al.*, 2013, 2014; *Duan et al.*, 2004; *Li et al.*, 2010; *Zhang et al.*, 2008, 2015]. For example, it was estimated that approximately 70% of organic carbon (OC) in June 1998 was from biomass burning [*Duan et al.*, 2004]. A more recent

study combining positive matrix factorization (PMF) and biomass burning markers (levoglucosan and K^+) showed that 50% of the OC and elemental carbon (EC) in Beijing were associated with biomass burning processes [*Cheng et al*., 2013]. These results suggest that the contribution of biomass burning to PM pollution is significant and can vary substantially year by year. However, most previous analyses were based on filter measurements, our knowledge of the rapid evolution of biomass burning aerosol remains less understood. In recent years, the real-time online technique, e.g., aerosol mass spectrometers (AMS), with the subsequent PMF analysis were used to characterize biomass burning aerosol in different regions in China. For example, biomass burning organic aerosol (BBOA) was found to contribute 24.5% and 29.5% to OA at a rural and an urban site, respectively, in Pearl River Delta regions [*He et al*., 2011; *Huang et al*., 2011], and 36–39% during the summer wheat harvest and autumn rice harvest in the Yangtze River Delta (YRD) [*Zhang et al*., 2015]. Comparatively, few of AMS measurements were used to characterize biomass burning in the North China Plain. The properties of biomass burning aerosol, e.g., composition, optical properties, and hygroscopicity can have rapid changes in the atmosphere due to oxidation [*Vakkari et al*., 2014], thus, characterization of the evolution and aging of biomass burning aerosol is of importance for understanding its impacts on optical properties and PM pollution.

In this study, we present the results from a summer campaign that was conducted at Xianghe, a typical suburban site in the North China Plain with frequent influences of severe haze pollution [*Xin et al*., 2015]. In this work, submicron aerosol species, including organics, sulfate, nitrate, ammonium, chloride, black carbon (BC), gaseous species, and optical properties were measured in situ by an Aerodyne Aerosol Chemical Speciation Monitor (ACSM) along with a range of collocated instruments. The aerosol composition, diurnal cycles, and sources of OA are investigated. The life cycles of severe haze pollution episodes are elucidated in a case study. In addition, the biomass burning aerosol characteristics and its impact on optical properties are also discussed.

2. Experimental Method

2.1. Sampling Site

The sampling site is located at the Xianghe Atmospheric Observatory (39.798°N, 116.958°E; 15 m above sea level), which is approximately 50 km southeast of Beijing, 75 km northwest of Tianjing, and 35 km northeast of Langfang in Hebei province (Figure 1). The sampling site is approximately 4 km west of the downtown center (with a population of ~50,000) and is surrounded by agricultural land. Located between several megacities, the Xianghe site experiences frequent pollution plumes [*Xin et al*., 2015] and is subject to multiple source influences such as local emissions and regional transport from the urban areas.

2.2. Instrumentation

All the instruments were mounted in an air-conditioned container with the sampling height being approximately 4 m. The nonrefractory submicron aerosol (NR-PM_1) species including organics (Org), sulfate (SO_4), nitrate (NO_3), ammonium (NH_4), and chloride (Cl) were measured in situ by the ACSM at a time resolution of ~15 min. Ambient aerosols were drawn inside the container through a 1/2″ (outer diameter) stainless steel tube at a flow rate of ~3 L min^{-1}, of which ~0.1 L min^{-1} was isokinetically subsampled into the ACSM. A $PM_{2.5}$ cyclone (Model: URG-2000-30ED) was supplied in front of the sampling inlet to remove coarse particles larger than 2.5 μm. Aerosol particles were then dried by a silica gel diffusion dryer before sampling into the ACSM. Before the campaign, the ACSM was calibrated with pure ammonium nitrate particles following the standard protocols in *Ng et al*. [2011b]. The ionization efficiency and relative ionization efficiency of ammonium were determined.

Because ACSM is insensitive to refractory materials, e.g., BC and mineral dust at the vaporizer temperature of ~600°C, an Aethalometer (AE22, Magee Scientific Corp.) was used to measure light absorbing carbon (LAC) concentrations at 370 nm and 880 nm. The LAC measured at 880 nm was defined as BC. In addition, the absorption coefficients (b_{ap}) of $PM_{2.5}$ at three wavelengths (405, 532, and 781 nm) were measured simultaneously by a Photoacoustic Soot Spectrometer (PASS-3, Droplet Measurement Technologies). The size-dependent particle number concentrations in the range of 14–736 nm were measured by a Scanning Mobility Particle Sizer Spectrometer (SMPS, Model 3081, TSI). The gaseous species including CO (Model 45*i*), SO_2 (Model 43*i*), NO/NO_2 (Model 42*i*), and O_3 (Model 49*i*) were measured by a series of gas analyzers from the Thermo Scientific. The ambient visibility was measured by a Visibility Sensor (Model 6000, BELFORT). The meteorological parameters including temperature (*T*), relative humidity

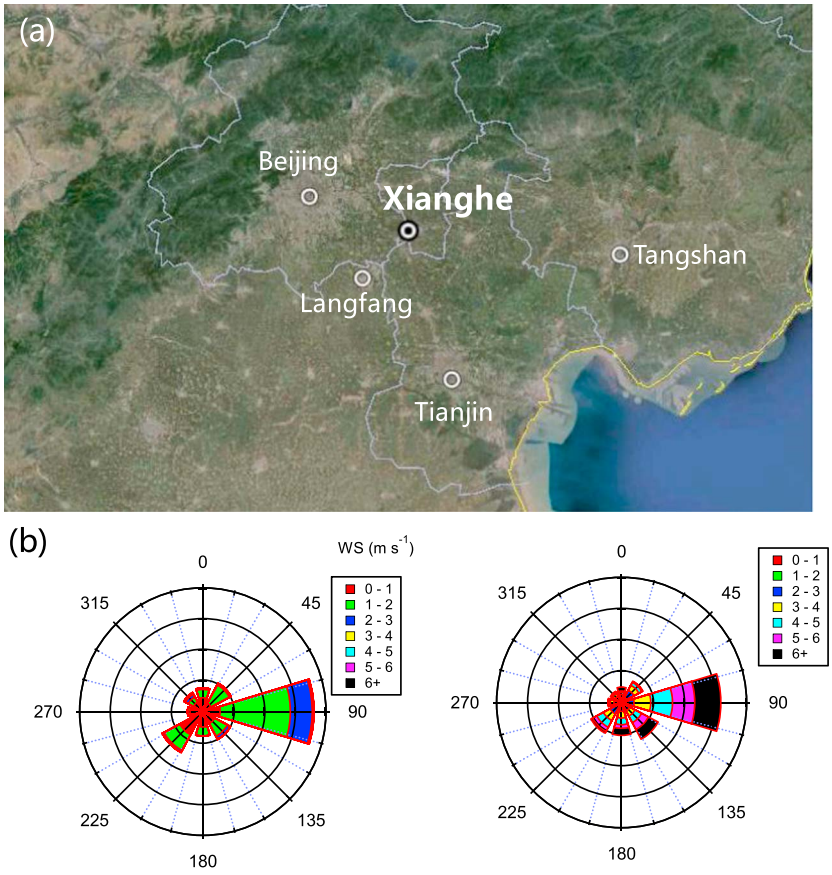

Figure 1. (a) Map of the sampling site (Xianghe), and (b) wind rose plots for the entire study period at (left) ground site and (right) 100 m.

(RH), wind direction (WD), and wind speed (WS) at seven heights (8, 15, 32, 47, 65, 80, and 100 m) were obtained from the Xianghe 102 m meteorological tower nearby. In addition, the data of solar radiation and precipitation were obtained from the ground meteorological station at the sampling site. During the study period, the campaign area was generally hot and moist with an average RH of 71.9% and an average *T* of 23.5°C (Figure 2). The prevailing wind was from the east (Figure 1b). All the data in this study are reported at ambient conditions in Beijing Standard Time, which is equal to universal time coordinated plus 8 h.

2.3. ACSM Data Analysis

The ACSM data were analyzed for the mass concentrations of NR-PM_1 species using the ACSM standard data analysis software (v 1.5.3.0). A constant collection efficiency (CE) of 0.5, commonly applicable in field campaigns [*Canagaratna et al*., 2007] was used in this study because (1) aerosol particles were dried before sampling into the ACSM, (2) the average ratio of measured NH_4 to predicted NH_4 that requires to fully neutralize SO_4, NO_3, and Cl [*Zhang et al*., 2007] was approximately 0.81 (Figure S1 in the supporting information), and (3) the mass fraction of ammonium nitrate was generally below 45%. Therefore, RH, particle acidity, and the mass fraction of ammonium nitrate could not affect CE significantly [*Middlebrook et al*., 2012]. Indeed, the particle volumes converted from the ACSM mass using the estimated particle density on the basis of chemical composition of PM_1 [*Salcedo et al*., 2006] agreed well with those determined from the SMPS measurements ($r^2 = 0.85$, slope = 0.97, Figure S2), supporting that CE = 0.5 was reasonable in this study.

Positive matrix factorization (PMF) [*Paatero and Tapper*, 1994] was performed on the ACSM OA mass spectra between *m/z* 12 and *m/z* 120 to resolve potential OA factors with different sources and processes. The detailed procedures for PMF analysis of the ACSM data set have been given in *Ng et al*. [2011b] and *Sun*

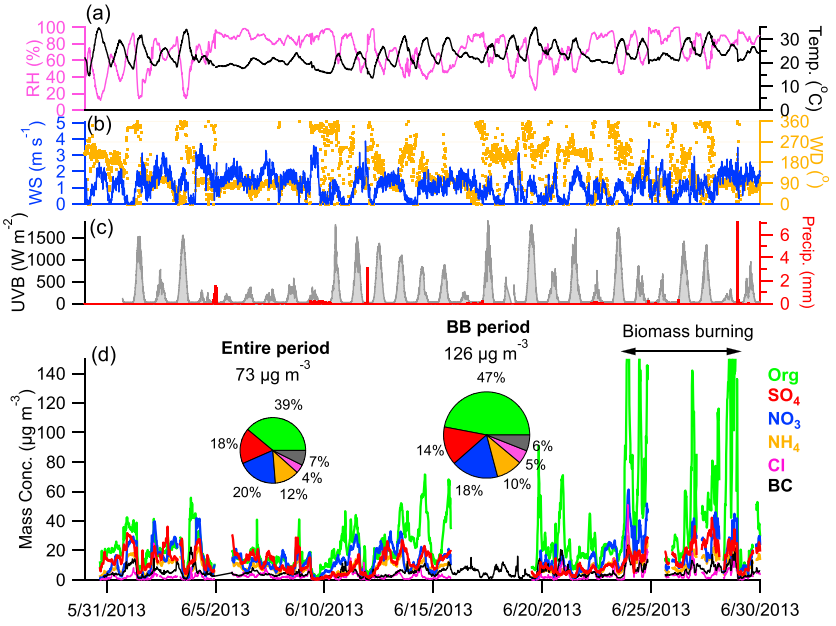

Figure 2. Time series of (a) temperature (*T*) and relative humidity (RH), (b) wind speed (WS) and wind direction (WD), (c) solar radiation and precipitation, and (d) submicron aerosol species during the study period. The two pie charts show the average chemical composition of PM_1 for the entire period and biomass burning (BB) period.

et al. [2012]. The PMF results were evaluated following the steps recommended by *Zhang et al.* [2011] with a PMF diagnostics tool written in Igor Pro [*Ulbrich et al.*, 2009]. Four OA factors including a hydrocarbon-like OA (HOA), a biomass burning OA (BBOA), a semivolatile oxygenated OA (SV-OOA), and a low-volatility OOA (LV-OOA) were identified. The detailed descriptions for the selection of PMF factors and key diagnostic plots for the PMF solution are provided in the supporting information.

2.4. FLEXPART Analysis

The footprint regions of the sampling site were determined by 2 day backward simulations of particles dispersion based on the Lagrangian particle dispersion model FLEXPART [*Stohl et al.*, 2005] coupled with the Weather Research and Forecasting (WRF) model [*Skamarock et al.*, 2005]. In this study, the FLEXPART model was driven by meteorological field (spatial resolution = 10 km, time resolution = 1 h) that was simulated by WRF. In simulations, 10,000 tracer particles were released from the site at a height of 50 m and the model was run backwardly to determine the source areas and transport pathways of air pollutants during the specified period.

3. Results and Discussion

3.1. Mass Concentrations and Diurnal Variations

PM_1 varied substantially across the entire study with the mass concentration ranging from 3.9 to 426 $\mu g\,m^{-3}$. The average ($\pm 1\sigma$) mass concentration was 73 (± 49) $\mu g\,m^{-3}$, which is nearly 40% higher than that observed in Beijing in summer 2011 (July and August) [*Sun et al.*, 2012], yet it was similar to that observed in June 2012 [*Sun et al.*, 2015]. As indicated in Figure 2d, the variations of submicron aerosol species were also dramatic, particularly for organics during the late period of this study. For instance, the mass concentration of organics rapidly increased from $<20\,\mu g\,m^{-3}$ to $247\,\mu g\,m^{-3}$ on 23 June due to the impact of agricultural burning. Overall, organics dominated the total PM_1 mass, on average accounting for 39%. Secondary inorganic aerosol (SIA = sulfate + nitrate + ammonium) together accounted for 50% of the total PM_1 with comparable contributions of sulfate (18%) and nitrate (20%). Such an averaged composition of PM_1 at the suburban site was overall similar to that previously reported in summer in Beijing [*Sun et al.*, 2010, 2012].

The diurnal cycles varied differently among different aerosol species. Organics presented a relatively flat diurnal pattern with higher concentration at nighttime. A clear nighttime peak between 20:00 and 21:00

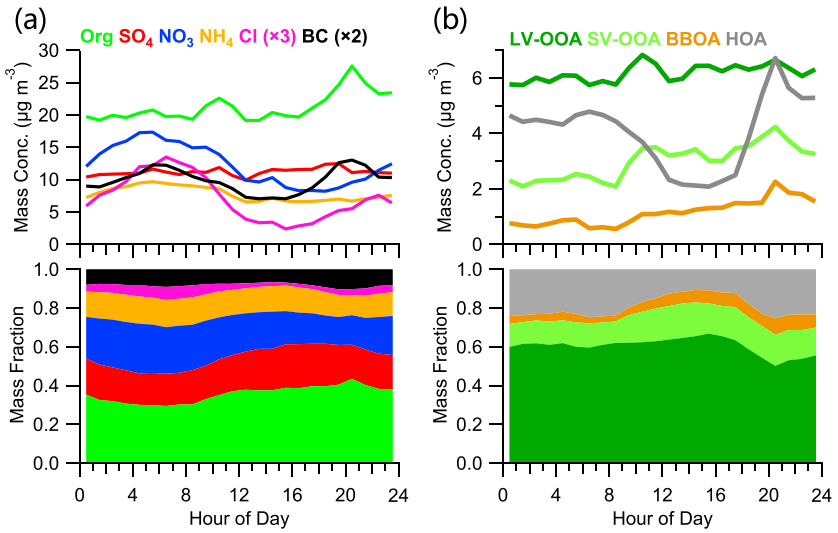

Figure 3. Diurnal cycles of mass concentrations and mass fractions of (a) submicron aerosol species and (b) OA factors by excluding the BB period indicated in Figure 2. The box-whisker plots of diurnal cycles of all species are shown in Figures S3 and S4.

was also observed, which was consistent with that of HOA (Figure 3b). Such a diurnal pattern was significantly different from that observed in the megacity of Beijing where organics often showed two pronounced peaks corresponding to meal times [*Huang et al*., 2010; *Sun et al*., 2010, 2012]. This result suggested that our sampling site was less influenced by local cooking emissions. After considering the dilution effect of planetary boundary layer (PBL) using ΔCO (CO by subtracting the background concentration of 0.544 ppm) as a reference tracer, Org/ΔCO showed a pronounced diurnal cycle with clear daytime increase (Figure S5), which is indicative of photochemical production. Note that high Org/ΔCO at nighttime was also likely caused by the enhanced primary emissions, e.g., HOA (Figure 3b). Similar to previous studies in Beijing, the diurnal cycle of sulfate was flat throughout the day indicating the regional character of sulfate. SO_4/ΔCO presented a gradual increase from early morning to late afternoon (Figure S5) indicating that the gas-phase photochemical production of sulfate during daytime also played a role. Nitrate and chloride showed similar diurnal cycles with much lower concentrations during daytime than nighttime. Such diurnal cycles were mainly caused by the gas-particle partitioning of semivolatile ammonium nitrate and ammonium chloride associated with temperature. High *T* during daytime facilitates the transformation of these two species from particle phase to gaseous HNO_3 and HCl [*Hu et al*., 2008] and hence leads to low particle concentrations during daytime. Compared to the decrease of Cl/ΔCO, NO_3/ΔCO showed relatively constant concentration during daytime, highlighting a competitive effect of daytime photochemical production versus evaporative loss in driving the diurnal cycle of nitrate. BC presented two pronounced peaks occurring in early morning and evening rush hours, indicating the contributions of traffic emissions. The diurnal aerosol composition varied across different time of the day. Overall, organics dominated PM_1 throughout the day, varying from 30 to 45%. Sulfate contributed 17–23% of PM_1 with the highest contribution occurring at ~16:00. Comparatively, nitrate presented the highest contribution (26%) at ~4:00 when *T* was the lowest and RH was the highest in a day. Chloride and BC generally contributed small fractions of PM_1 with higher contributions observed at night.

Liquid water was shown to play a significant role in aerosol processing during wintertime [*Sun et al*., 2013a]. Here the variations of aerosol mass concentrations and compositions as a function of RH are shown in Figure 4. The mass concentrations of organics and sulfate showed almost linear increases at low RH levels (<50%) and then remained at relative constant values between 50 and 80%. As a comparison, nitrate and chloride continued to show large increases in the RH range of 50–80%, suggesting a stronger impact of RH on these two species. One explanation was the high liquid water content that facilitated the transformation of gaseous HNO_3 and HCl into aqueous-phase particles. This is consistent with the results from a recent study in Los Angeles, that the particle/gas ratio of nitric acid was observed to have a large increase as a function of ambient RH [*Liu et al*., 2012]. Another explanation is that higher RH periods generally occur at nighttime with lower *T*, which also facilitated the gas-particle partitioning of semivolatile nitrate and chloride. All aerosol

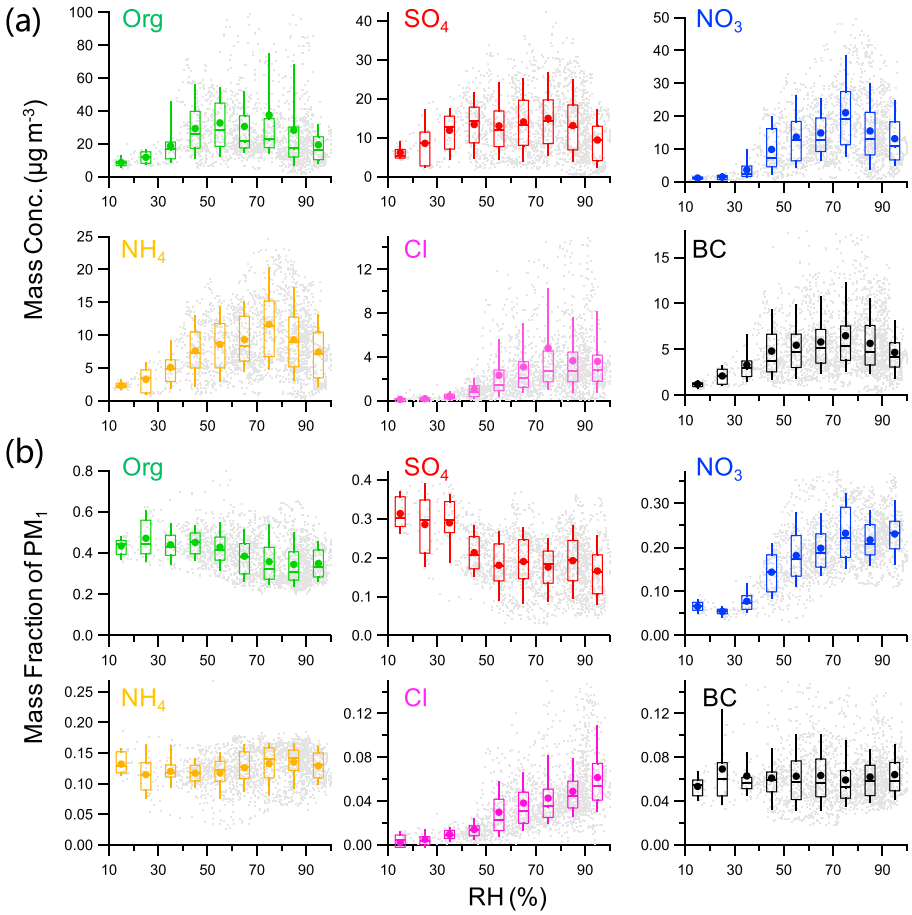

Figure 4. Variations of mass concentrations and mass fraction of submicron aerosol species as a function of RH. The data are grouped in RH bins (10% increment), and the median (middle horizontal line), mean (solid circles), 25th and 75th percentiles (bottom and top boxes), and 10th and 90th percentiles (bottom and top whiskers) are shown for each bin.

species showed decreases as RH was above 80%, which was mainly due to the scavenging by the precipitation. Because of the different impacts of RH on different aerosol species, the aerosol composition varied substantially as a function of RH. While the contribution of sulfate to PM_1 decreased from ~30% to ~20% as RH increased to >50%, that of nitrate showed a significant increase from ~5% to 25%. These results indicated that nitrate played an enhanced role in PM pollution at high RH levels. The RH dependence of sulfate and nitrate was quite different from that in winter [*Sun et al.*, 2013a]. During wintertime, sulfate was found to show an elevated contribution to PM_1 at high RH levels due to aqueous-phase production, whereas the nitrate contribution showed much smaller variations at different RH levels [*Sun et al.*, 2013a]. Such differences illustrated the different roles of formation mechanisms associated with particle liquid water between summer and winter. The contribution of chloride showed similar RH dependence as nitrate, indicating that the gas-particle partitioning associated with liquid water has played the dominant role. The contribution of BC appeared to be less affected by RH and showed a relatively constant fraction across different RH levels.

3.2. Composition and Sources of Organic Aerosol

PMF analysis of OA mass spectra resolved four OA factors including HOA, BBOA, SV-OOA, and LV-OOA. The HOA spectrum resembled that of diesel exhaust [*Canagaratna et al.*, 2004] and those resolved at various urban sites [*Ng et al.*, 2011a], which was characterized by the hydrocarbon ion series of $C_nH_{2n-1}^+$ and $C_nH_{2n+1}^+$. HOA correlated with BC—a tracer for combustion emissions during nonbiomass burning (NBB) period ($r^2 = 0.44$). The average ratio of HOA/BC was 0.91 which was lower than that (~1.2–1.3) observed in other megacities, e.g., New York City [*Sun et al.*, 2011] and Mexico City [*Aiken et al.*, 2009]. However, the average HOA/BC ratio fell within the values from light-duty vehicles and diesel trucks emission, which were 1.4 and

0.5, respectively [*Ban-Weiss et al*., 2008]. These results might suggest a mixed primary traffic emissions from gasoline and diesel vehicles near our sampling site. HOA showed a pronounced diurnal cycle with the nighttime concentration more than twice higher than that during daytime (Figure 3b). Such a diurnal cycle was remarkably similar to the traffic-related HOA resolved by a high-resolution aerosol mass spectrometer (HR-AMS) during the 2008 Beijing Olympic Games [*Huang et al*., 2010]. Note that the traffic-related HOA and COA often cannot be separated by quadrupole aerosol mass spectrometer due to its low sensitivity and low mass resolution, for instance, in summer in Beijing [*Sun et al*., 2010, 2012]. As a result, the diurnal cycles of HOA in *Sun et al*. [2010] and *Sun et al*. [2012] showed two pronounced peaks corresponding to meal times due to significant influences from cooking emissions. Given the significantly different diurnal cycle of HOA in this study, we concluded that HOA at Xianghe was dominantly contributed by traffic emissions with fewer influences from cooking activities. The HOA on average contributed 19% of the total OA, which was similar to that reported in Beijing [*Huang et al*., 2010].

The mass spectrum of BBOA was characterized by the prominent peaks of *m/z* 60 and 73, two marker *m/z*'s indicative of biomass burning [*Aiken et al*., 2009; *Alfarra et al*., 2007; *Mohr et al*., 2009]. Not surprisingly, BBOA correlated tightly with *m/z* 60 ($r^2 = 0.97$), a major fragment *m/z* of anhydrosugars, e.g., levoglucosan [*Lee et al*., 2010]. Note that the BBOA spectrum showed higher f_{44} (fraction of *m/z* 44 in OA), a parameter indicative of the oxidation degree of OA [*Aiken et al*., 2008], compared to that observed in Yangtze River Delta (YRD) in summer 2013 [*Zhang et al*., 2015] and also that of fresh BBOA [*Aiken et al*., 2009], indicating that BBOA was relatively oxidized in this study. Recent lab and field experiments have found that biomass burning aerosol can have rapid changes in several hours due to atmospheric oxidation [*Hennigan et al*., 2010; *Vakkari et al*., 2014]. Thus, high f_{44} might suggest that BBOA in this study has been aged to a certain degree during the transport to the sampling site. Note that high *m/z* 44 in the BBOA spectrum may be also partly due to the ACSM that tends to produce higher *m/z* 44 than HR-AMS [*Crenn et al*., 2015]. As shown in Figure 5, BBOA showed much higher concentration during 23–29 June than other periods, indicating a considerable impact of agricultural burning during this period. In fact, BBOA contributed a small fraction of OA throughout the day (3–8.5%) during the periods in the absence of biomass burning (Figure 3b), whereas the average contribution was elevated to 21% during the BB period.

The two secondary OA (SOA) factors were both characterized by high *m/z* 44, and their mass spectra resemble those of standard OOA and LV-OOA reported previously [*Ng et al*., 2011a], yet with overall higher f_{44}. One of the reasons is that the ACSM measurements are subject to produce higher *m/z* 44 than those from HR-AMS [*Fröhlich et al*., 2015]. LV-OOA showed higher f_{44} than SV-OOA, indicating that LV-OOA was a more aged OA factor. LV-OOA correlated well with the sum of sulfate and nitrate during the NBB period ($r^2 = 0.51$), and the average ratio of LV-OOA/($SO_4 + NO_3$) (0.45) was also similar to that observed in summer in Beijing [*Huang et al*., 2010; *Sun et al*., 2010, 2012]. The diurnal cycle of LV-OOA was relatively flat indicating that LV-OOA was a regional processed factor. Comparatively, the SV-OOA concentration was significantly elevated during the BB period while remaining at relatively low levels during the rest of the time. These results likely indicated that a considerable fraction of SV-OOA during the BB period was from the oxidized BBOA. In fact, the SV-OOA spectrum was remarkably similar to that of OOA-BB, a factor indicative of oxidized BBOA that was resolved in summer in YRD region [*Zhang et al*., 2015]. The SOA together contributed 70% of OA with LV-OOA and SV-OOA being 52% and 18%, respectively. The SOA contribution was even higher than that (~60%) observed in summer in Beijing [*Sun et al*., 2010, 2012], indicating the significance of secondary formation during this study.

3.3. Biomass Burning Aerosol

We observed strong biomass burning events during 23–29 June (Figures 2 and 5), consistent with the ubiquitous fire spots in the North China Plain during this period (Figure S6). The average PM_1 concentration during the BB period was 124 $\mu g\, m^{-3}$, which was approximately twice that of the NBB period (Table 1). This result indicated that biomass burning is a large source of PM pollution and could contribute approximately 50% of the total fine particle mass. While all submicron aerosol species showed large increases during the BB period, organics and chloride presented the largest increase by a factor of 2.6–2.7. This is consistent with the dominant emissions of carbonaceous materials and chloride from biomass burning [*Hays et al*., 2005; *Levin et al*., 2010]. Similarly large increases of OC and Cl during BB episodes were also observed in Beijing [*Cheng et al*., 2013]. Aerosol composition had substantial changes during the BB period. The submicron

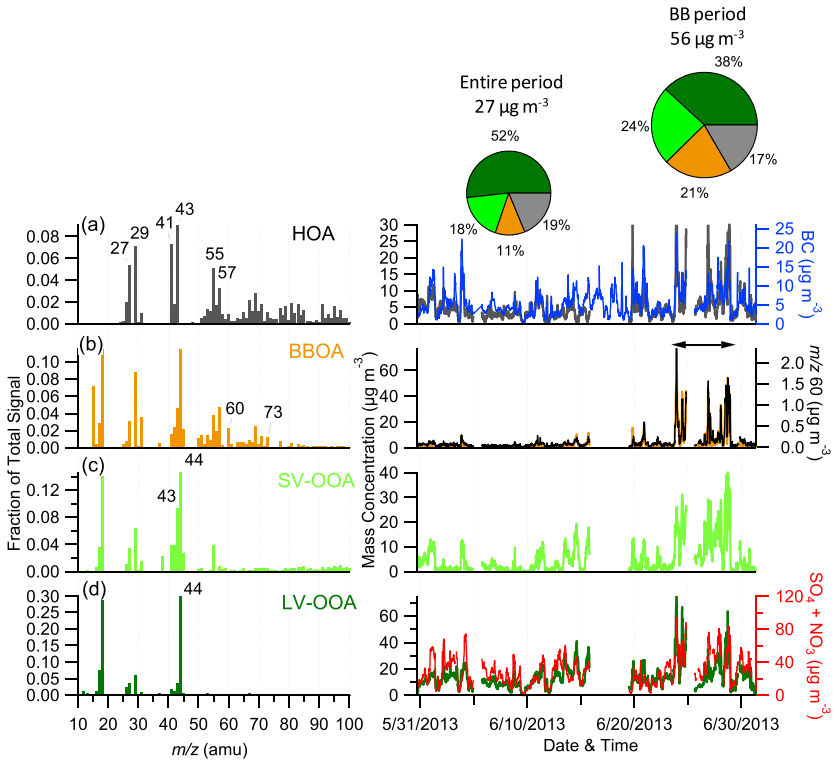

Figure 5. (left column) Mass spectra and (right column) time series of the four OA factors, i.e., HOA, BBOA, SV-OOA, and LV-OOA. Also shown in Figure 5 (right column) is the time series of external tracers including BC, *m/z* 60 and the sum of SO_4 and NO_3. The two pie charts show the average OA composition for the entire period and the BB period.

aerosol during the BB period was mainly composed of organics, accounting for 48% on average, followed by nitrate (18%) and sulfate (15%). While the contributions of organics and chloride were increased by approximately 30%, those of SIA showed corresponding decreases. Such compositional changes exert potential impacts on aerosol hygroscopic properties and cloud condensation nuclei given that biomass burning aerosols are often less hygroscopic than SIA [*Petters et al.*, 2009]. In fact, *F. Zhang et al.* [2014] observed a clear decrease of hygroscopicity parameter (kappa) and activation ratio of particles during the BB period in this study.

BBOA showed the largest increase by a factor of 10 from 1.2 $\mu g\,m^{-3}$ during the NBB period to 11.8 $\mu g\,m^{-3}$ during the BB period. The contribution of BBOA to OA showed a corresponding increase from 5.6% to 21%. Although the LV-OOA and HOA concentrations were also elevated by a factor of 1.7 and 2.3, respectively, the enhancement ratios were much lower than that of BBOA suggesting the much smaller impacts of BB on these two species. It should be noted that the SV-OOA concentration was increased by a factor of ~5 from 3.0 to 13.7 $\mu g\,m^{-3}$ during the BB period, and correspondingly, its contribution to OA increased from 14% to 24%. These results supported our conclusion that a considerable fraction of SV-OOA was likely from the oxidized biomass burning aerosols. The evolution of BB aerosol can be illustrated by the scatter plot of f_{44} versus f_{60} (fraction of *m/z* 60) [*Cubison et al.*, 2011]. As indicated in

Table 1. A Summary of the Average Mass Concentrations ($\mu g\,m^{-3}$) of Aerosol Species for the Entire Study Period and Also the Periods With and Without Influences of BB[a]

	Entire	BB	NBB	BB/NBB
Org	28.3	59.2	21.7	2.7
SO_4	12.8	18.2	11.6	1.6
NO_3	14.3	22.3	12.6	1.8
NH_4	8.8	12.4	8.0	1.5
Cl	3.1	6.4	2.4	2.6
BC	5.4	7.5	4.9	1.5
PM_1	72.6	125.9	61.2	2.1
LV-OOA	14.1	21.5	12.5	1.7
SV-OOA	4.9	13.7	3.0	4.6
BBOA	3.1	11.8	1.2	10.2
HOA	5.1	9.4	4.1	2.3

[a]Also shown is the average enhancement ratio of aerosol species during the BB period compared to the NBB period.

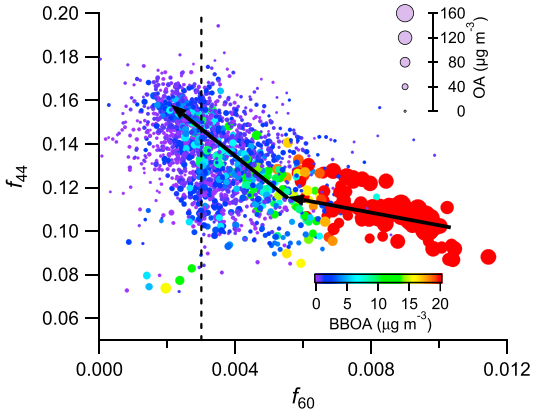

Figure 6. Scatter plot of f_{44} versus f_{60} for the entire study. The nominal background value of 0.3% is shown by the vertical dashed line. The two arrow lines are shown as visual references for the aging of biomass burning aerosols.

Figure 6, f_{60} during the BB period was well above ~0.3%, a typical value in the absence of biomass burning [*Cubison et al.*, 2011]. As the BB aerosol was aged, f_{60} was rapidly decreased from ~0.01 to 0.004. As a consequence, aerosol became more oxidized associated with an increase of f_{44} from approximately 0.10 to 0.14. The aging of BB aerosol is subject to be rapid [*Hennigan et al.*, 2011], which can lead to substantial secondary aerosol formation and also changes in optical and hygroscopic properties in hours [*Vakkari et al.*, 2014].

Figure 7a shows a comparison between the absorption coefficient (b_{ap}) measured by the PASS-3 and the LAC measured by the Aethalometer. While b_{ap} highly correlated with BC (880 nm) during both NBB ($r^2 = 0.92$) and BB ($r^2 = 0.89$) periods, the mass absorption efficiency (MAE) used to convert BC to the b_{ap} at 532 nm was 9.41 $m^2 g^{-1}$ during the BB period, which was higher than that during the NBB period (8.86 $m^2 g^{-1}$), indicating an increase of MAE due to the BB impacts. The MAE during the NBB period was close to that (8.28 $m^2 g^{-1}$) reported previously in Beijing [*Yan et al.*, 2008]. As shown in Figure 7b, the average ratio of $b_{ap,\ 405nm}/b_{ap,\ 781nm}$ during the BB period was approximately 60% higher than that during the NBB period, which indicated a large enhancement of absorption due to non-BC sources. This is consistent with the results from previous studies that certain organic compounds from biomass burning emissions can absorb strongly in the ultraviolet and short-wavelength visible region [*Desyaterik et al.*, 2013; *Laskin et al.*, 2015]. The LAC measured at 370 nm showed similar enhancement by 62% compared to that measured at 880 nm. These results suggest that agricultural burning emissions have a considerable impact on aerosol optical properties, particularly in the ultraviolet region. Therefore, climate models need to consider the biomass burning impacts in harvest seasons when modeling the radiative forcing of aerosol particles in China.

3.4. Case Study of Haze Life Cycle

Figure 8 presents a case study elucidating a complete life cycle of haze episode. The evolution of the haze episode (Ep1) can be classified into four stages, which were stage 1 (*S*1, 11:00–15:00, 1 June) representing a clean period before the episode, stage 2 (*S*2, 15:00–24:00, 1 June) representing the formation stage of the episode, stage 3 (*S*3, 0:00, 2 June to 10:00, 3 June) representing the haze episode with high concentrations of fine particles, and stage 4 (*S*4, 10:00–15:00, 3 June) representing the clean of haze episode. During the clean stage *S*1, RH was low (~20%) and the winds were dominantly from the north (Figures 8a and 8b). The footprint analysis also showed that air masses were mainly from the northwest (Figure 9a). Under such meteorological conditions, all aerosol species presented low mass concentrations with the total PM_1

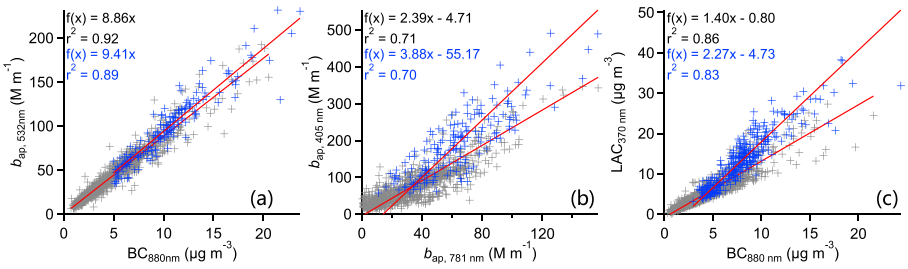

Figure 7. Scatter plots of (a) absorption coefficient (b_{ap}, 532 nm) versus BC, (b) b_{ap} measured at 405 nm and 781 nm, and (c) LAC measured at 370 nm and BC at 880 nm, during the BB (blue) and NBB (gray) periods.

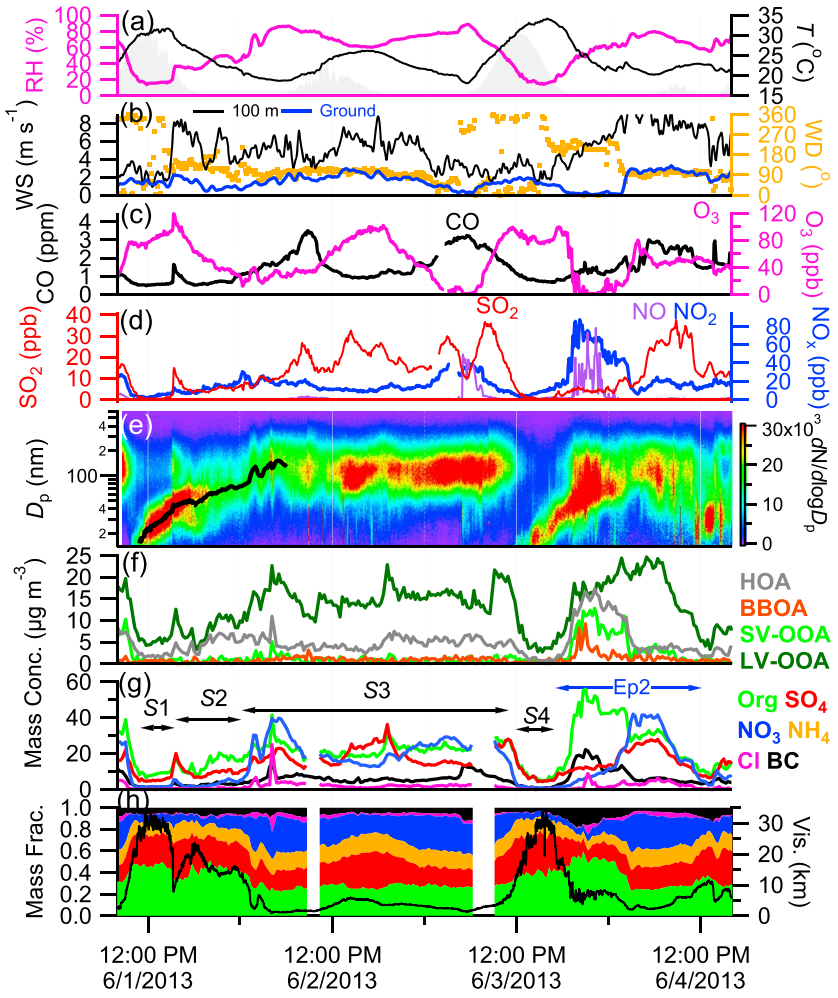

Figure 8. Evolution of (a, b) meteorological parameters, (c, d) gaseous species, (e) size distributions of particle number concentrations, (f) OA factors, and (g, h) submicron aerosol species in the case study during 1–4 June 2013.

concentration less than 20 $\mu g\,m^{-3}$, leading to a good visibility at approximately 30 km. Organics dominated the total PM_1 mass accounting for ~45%, followed by sulfate (~30%). A clear new particle growth event was also observed during this stage (Figure 8e), and the aerosol particle size grew from ~15 nm to ~40 nm within 4 h with an average particle grow rate of ~6 $nm\,h^{-1}$.

The wind direction was changed from the north to the east at ~15:00, which was associated with a sudden increase of RH and wind speed at 100 m. RH increased gradually during *S2* while *T* decreased instead. It should be noted that the ground WS remained at low values ($<2\,m\,s^{-1}$) during this stage, whereas it was relatively high ($>4\,m\,s^{-1}$) at 100 m (Figure 8b). Such meteorological conditions facilitated the regional transport at a higher altitude. For example, the regional LV-OOA and sulfate showed clear increases during this stage, whereas the local traffic-related CO, NO, and BC remained relatively constant, indicating that regional transport started to play a role in the PM evolution during *S2*. Aerosol particles continued to grow with the largest geometric mean diameter reaching 75 nm, and the concentration of PM_1 increased from ~20 $\mu g\,m^{-3}$ to ~40 $\mu g\,m^{-3}$, leading to a significant reduction of the visibility from 20 km to ~10 km. The footprints showed a change from the northwest to the southeast during this stage suggesting that the pollution was mainly transported from the southeast (Figure 9b).

Aerosol composition had a substantial change after midnight on 1 June, mainly due to the sudden increase of nitrate from ~5 $\mu g\,m^{-3}$ to ~40 $\mu g\,m^{-3}$ in 2 h (Figure 8g). Such an increase was associated with the similar increase of RH, which likely facilitated the gas-particle partitioning of HNO_3 and/or nighttime heterogeneous

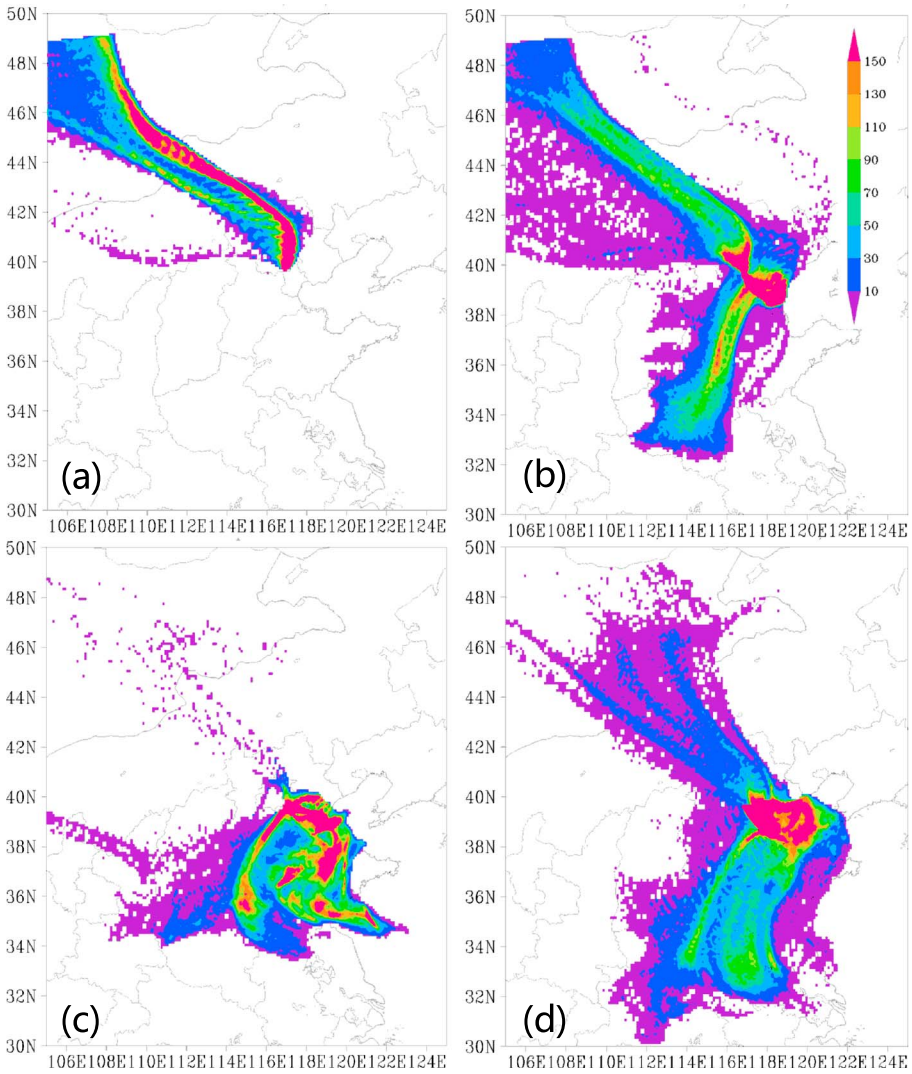

Figure 9. Footprint regions of the periods of (a) *S*1, (b) *S*2, (c) *S*3, and (d) Ep2, which are marked in Figure 8. The legend indicates the number concentrations of tracer particles.

reactions in the nitrate formation. The contribution of organics decreased from more than 40% to less than 25%, and the SIA contribution showed a corresponding increase to ~70% (Figure 8h), indicating that SIA played an enhanced role in the severe haze episode. The meteorology was stagnant with consistently high RH (60–80%) and dominant winds from the east. The mass loadings of submicron aerosol species remained at high levels during the entire stage of *S*3 with higher contribution of nitrate at nighttime and higher contribution of sulfate during daytime. Note that SO_2 during *S*3 was ~10–30 ppb, which was significantly higher than that (~5 ppb) during *S*2 (Figure 8d). Given that there was no large point source of SO_2 at the Xianghe site, high concentration of SO_2 was inferred mainly from regional transport. Another support was the relatively high wind speed at both 100 m ($>4\ m\ s^{-1}$) and the ground site ($\sim 2\ m\ s^{-1}$). The footprint analysis also highlighted that the major source areas of *S*3 were located to the southeast (Shandong province) and the southwest (Hebei province) of the sampling site over a regional scale (Figure 9c). These results together illustrated that the haze episode of *S*3 was mainly formed regionally. Additional support was the low NO from the local emissions and the consistently large accumulation mode particles (~100 nm) during *S*3 (Figure 8).

The haze episode of *S*3 was cleaned by a switch of wind direction from the east to the north. The clean process (*S*4) was rapid with the concentration of PM_1 decreasing from 80 to $<20\ \mu g\ m^{-3}$ in 2 h. As a result, the visibility rapidly increased from ~3 km to >20 km. However, the clean period was short, only lasting ~3 h. After that, another haze episode (Ep2) with significantly different aerosol composition from Ep1 was formed.

The formation of Ep2 was associated with a wind direction change from the north to the south. Organics and BC presented the largest increases among submicron aerosol species, and NO/NO_2 also showed dramatic increases during this stage (Figures 8d and 8g). Given the stagnant meteorological conditions as indicated by the zero wind speed at the ground level, the formation of Ep2 was primarily contributed by local source emissions. The footprint analysis in Figure 9d also showed that the aerosol particle sources were mainly located in small areas near Xianghe site. As the wind direction was changed to the east at 0:00 on 4 June, the meteorological conditions, gaseous concentrations, and aerosol composition during the subsequent episode were much similar to those of *S*3, likely indicating the circulation of the previous regional haze episode of *S*3 to the south of Xianghe, which was not cleaned by the short period of air masses changes during *S*4. Overall, the case study analysis revealed two different haze life cycles. While the formation of the two episodes were both initiated by the changes of meteorological conditions, the first type of episode was mainly formed regionally with substantially enhanced contributions of secondary aerosol species, and the second type of episode was dominantly from local sources with high contributions of organics and BC.

4. Conclusions

We have characterized the chemical composition, sources, and processes of submicron aerosols at a suburban site in the North China Plain in June 2013. The average ($\pm 1\sigma$) PM_1 concentration was 73 (± 49) $\mu g\ m^{-3}$ during the study period indicating that the suburban site was as heavily polluted as megacities. The submicron aerosol composition was also similar to that observed in the megacity of Beijing, which was mainly composed of organics, on average accounting for 39%, followed by nitrate (20%) and sulfate (18%). Aerosol composition had a substantial change during the BB period which was characterized by a significant enhancement of organics (48%) and chloride. Positive matrix factorization of OA spectra identified four OA factors from traffic emissions (HOA), biomass burning emissions (BBOA), and secondary formation (SV-OOA and LV-OOA). The OA was dominated by SOA (SV-OOA + LV-OOA), on average accounting for 70%, with a considerable contribution from BBOA (11%). The contribution of BBOA to OA was significantly elevated to 21% during the BB period. Biomass burning was also found to have a large impact on aerosol absorption properties. It was estimated that ~60% enhancement of absorption coefficient at ultraviolet spectral region during the BB period was caused by biomass burning emissions. We also have investigated the formation and evolution mechanisms of severe haze episodes in a case study. Our analysis highlighted two different haze life cycles that were driven by regional transport and local source emissions, respectively. While the severe haze pollution from regional transport was dominated by secondary aerosols (SIA + SOA), it was mainly comprised of organics and BC when local sources were dominant. Liquid water played a significant role in the formation of severe haze pollution, particularly exerting large impacts on nitrate and chloride due to the transformation of gaseous acids into the liquid particles under high RH conditions.

Acknowledgments
This work was supported by the Strategic Priority Research Program (B) of the Chinese Academy of Sciences (XDB05020501), the National Key Project of Basic Research (2013CB955801), and open fund by Jiangsu Key Laboratory of Atmospheric Environment Monitoring and Pollution Control (KHK1301), a project funded by the Priority Academic Program Development of Jiangsu Higher Education Institutions (PAPD). We thank Xiaole Pan, Qingqing Wang, Huabin Dong, Weidong Nan, Li Sun, and Qingli Wang for their assistance during the campaign. The observational data in this study are available from the authors upon request (sunyele@mail.iap.ac.cn).

References

Aiken, A. C., et al. (2008), O/C and OM/OC ratios of primary, secondary, and ambient organic aerosols with high-resolution time-of-flight aerosol mass spectrometry, *Environ. Sci. Technol.*, *42*(12), 4478–4485.

Aiken, A. C., et al. (2009), Mexico City aerosol analysis during MILAGRO using high resolution aerosol mass spectrometry at the urban supersite (T0)—Part 1: Fine particle composition and organic source apportionment, *Atmos. Chem. Phys.*, *9*(17), 6633–6653.

Alfarra, M. R., A. S. H. Prevot, S. Szidat, J. Sandradewi, S. Weimer, V. A. Lanz, D. Schreiber, M. Mohr, and U. Baltensperger (2007), Identification of the mass spectral signature of organic aerosols from wood burning emissions, *Environ. Sci. Technol.*, *41*(16), 5770–5777.

Ban-Weiss, G. A., J. P. McLaughlin, R. A. Harley, M. M. Lunden, T. W. Kirchstetter, A. J. Kean, A. W. Strawa, E. D. Stevenson, and G. R. Kendall (2008), Long-term changes in emissions of nitrogen oxides and particulate matter from on-road gasoline and diesel vehicles, *Atmos. Environ.*, *42*(2), 220–232, doi:10.1016/j.atmosenv.2007.09.049.

Canagaratna, M. R., et al. (2004), Chase studies of particulate emissions from in-use New York City vehicles, *Aerosol Sci. Technol.*, *38*, 555–573.

Canagaratna, M. R., et al. (2007), Chemical and microphysical characterization of aerosols via aerosol mass spectrometry, *Mass Spectrom. Rev.*, *26*, 185–222.

Cao, J., H. Xu, Q. Xu, B. Chen, and H. Kan (2012), Fine particulate matter constituents and cardiopulmonary mortality in a heavily polluted Chinese city, *Environ. Health Perspect.*, *120*(3), 373–378.

Chen, C., et al. (2015), Characteristics and sources of submicron aerosols above the urban canopy (260 m) in Beijing, China, during the 2014 APEC summit, *Atmos. Chem. Phys.*, *15*(22), 12,879–12,895, doi:10.5194/acp-15-12879-2015.

Cheng, Y., G. Engling, K. B. He, F. K. Duan, Y. L. Ma, Z. Y. Du, J. M. Liu, M. Zheng, and R. J. Weber (2013), Biomass burning contribution to Beijing aerosol, *Atmos. Chem. Phys.*, *13*(15), 7765–7781, doi:10.5194/acp-13-7765-2013.

Cheng, Z., et al. (2014), Impact of biomass burning on haze pollution in the Yangtze River Delta, China: A case study in summer 2011, *Atmos. Chem. Phys.*, *14*(9), 4573–4585, doi:10.5194/acp-14-4573-2014.

Crenn, V., et al. (2015), ACTRIS ACSM intercomparison—Part 1: Reproducibility of concentration and fragment results from 13 individual Quadrupole Aerosol Chemical Speciation Monitors (Q-ACSM) and consistency with co-located instruments, *Atmos. Meas. Tech.*, *8*(12), 5063–5087, doi:10.5194/amt-8-5063-2015.

Cubison, M. J., et al. (2011), Effects of aging on organic aerosol from open biomass burning smoke in aircraft and laboratory studies, *Atmos. Chem. Phys.*, *11*(23), 12,049–12,064, doi:10.5194/acp-11-12049-2011.

Desyaterik, Y., Y. Sun, X. Shen, T. Lee, X. Wang, T. Wang, and J. Collett (2013), Speciation of "brown" carbon in cloud water impacted by agricultural biomass burning in Eastern China, *J. Geophys. Res. Atmos.*, *118*, 7389–7399, doi:10.1002/jgrd.50561.

Duan, F., X. Liu, T. Yu, and H. Cachier (2004), Identification and estimate of biomass burning contribution to the urban aerosol organic carbon concentrations in Beijing, *Atmos. Environ.*, *38*(9), 1275–1282, doi:10.1016/j.atmosenv.2003.11.037.

Fröhlich, R., et al. (2015), ACTRIS ACSM intercomparison—Part 2: Intercomparison of ME-2 organic source apportionment results from 15 individual, co-located aerosol mass spectrometers, *Atmos. Meas. Tech.*, *8*(6), 2555–2576, doi:10.5194/amt-8-2555-2015.

Hays, M. D., P. M. Fine, C. D. Geron, M. J. Kleeman, and B. K. Gullett (2005), Open burning of agricultural biomass: Physical and chemical properties of particle-phase emissions, *Atmos. Environ.*, *39*(36), 6747–6764, doi:10.1016/j.atmosenv.2005.07.072.

He, L.-Y., X.-F. Huang, L. Xue, M. Hu, Y. Lin, J. Zheng, R. Zhang, and Y.-H. Zhang (2011), Submicron aerosol analysis and organic source apportionment in an urban atmosphere in Pearl River Delta of China using high-resolution aerosol mass spectrometry, *J. Geophys. Res.*, *116*, D12304, doi:10.1029/2010JD014566.

Hennigan, C. J., A. P. Sullivan, J. L. Collett, and A. L. Robinson (2010), Levoglucosan stability in biomass burning particles exposed to hydroxyl radicals, *Geophys. Res. Lett.*, *37*, L09806, doi:10.1029/2010GL043088.

Hennigan, C. J., et al. (2011), Chemical and physical transformations of organic aerosol from the photo-oxidation of open biomass burning emissions in an environmental chamber, *Atmos. Chem. Phys.*, *11*(15), 7669–7686, doi:10.5194/acp-11-7669-2011.

Hu, M., Z. Wu, J. Slanina, P. Lin, S. Liu, and L. Zeng (2008), Acidic gases, ammonia and water-soluble ions in $PM_{2.5}$ at a coastal site in the Pearl River Delta, China, *Atmos. Environ.*, *42*(25), 6310–6320, doi:10.1016/j.atmosenv.2008.02.015.

Huang, R.-J., et al. (2014), High secondary aerosol contribution to particulate pollution during haze events in China, *Nature*, *514*, 218–222, doi:10.1038/nature13774.

Huang, X. F., et al. (2010), Highly time-resolved chemical characterization of atmospheric submicron particles during 2008 Beijing Olympic Games using an Aerodyne High-Resolution Aerosol Mass Spectrometer, *Atmos. Chem. Phys.*, *10*(18), 8933–8945, doi:10.5194/acp-10-8933-2010.

Huang, X. F., et al. (2011), Characterization of submicron aerosols at a rural site in Pearl River Delta of China using an Aerodyne High-Resolution Aerosol Mass Spectrometer, *Atmos. Chem. Phys.*, *11*(5), 1865–1877, doi:10.5194/acp-11-1865-2011.

Jiang, Q., Y. L. Sun, Z. Wang, and Y. Yin (2015), Aerosol composition and sources during the Chinese Spring Festival: Fireworks, secondary aerosol, and holiday effects, *Atmos. Chem. Phys.*, *15*(11), 6023–6034, doi:10.5194/acp-15-6023-2015.

Laskin, A., J. Laskin, and S. A. Nizkorodov (2015), Chemistry of atmospheric brown carbon, *Chem. Rev.*, doi:10.1021/cr5006167.

Lee, T., et al. (2010), Chemical smoke marker emissions during flaming and smoldering phases of laboratory open burning of wildland fuels, *Aerosol Sci. Technol.*, *44*(9), 1–5.

Levin, E. J. T., et al. (2010), Biomass burning smoke aerosol properties measured during Fire Laboratory at Missoula Experiments (FLAME), *J. Geophys. Res.*, *115*, D18210, doi:10.1029/2009JD013601.

Li, W. J., L. Y. Shao, and P. R. Buseck (2010), Haze types in Beijing and the influence of agricultural biomass burning, *Atmos. Chem. Phys.*, *10*(17), 8119–8130, doi:10.5194/acp-10-8119-2010.

Liu, J., et al. (2012), On the gas-particle partitioning of soluble organic aerosol in two urban atmospheres with contrasting emissions: 2. Gas and particle phase formic acid, *J. Geophys. Res.*, *117*, D00V21, doi:10.1029/2012JD017912.

Liu, X. G., et al. (2013), Formation and evolution mechanism of regional haze: A case study in the megacity Beijing, China, *Atmos. Chem. Phys.*, *13*(9), 4501–4514, doi:10.5194/acp-13-4501-2013.

Middlebrook, A. M., R. Bahreini, J. L. Jimenez, and M. R. Canagaratna (2012), Evaluation of composition-dependent collection efficiencies for the Aerodyne Aerosol Mass Spectrometer using field data, *Aerosol Sci. Technol.*, *46*, 258–271.

Mohr, C., J. A. Huffman, M. J. Cubison, A. C. Aiken, K. S. Docherty, J. R. Kimmel, I. M. Ulbrich, M. Hannigan, and J. L. Jimenez (2009), Characterization of primary organic aerosol emissions from meat cooking, trash burning, and motor vehicles with High-Resolution Aerosol Mass Spectrometry and comparison with ambient and chamber observations, *Environ. Sci. Technol.*, *43*(7), 2443–2449, doi:10.1021/es8011518.

Ng, N. L., M. R. Canagaratna, J. L. Jimenez, Q. Zhang, I. M. Ulbrich, and D. R. Worsnop (2011a), Real-time methods for estimating organic component mass concentrations from Aerosol Mass Spectrometer data, *Environ. Sci. Technol.*, *45*, 910–916, doi:10.1021/es102951k.

Ng, N. L., et al. (2011b), An Aerosol Chemical Speciation Monitor (ACSM) for routine monitoring of the composition and mass concentrations of ambient aerosol, *Aerosol Sci. Technol.*, *45*(7), 770–784.

Paatero, P., and U. Tapper (1994), Positive matrix factorization: A non-negative factor model with optimal utilization of error estimates of data values, *Environmetrics*, *5*, 111–126.

Petters, M. D., C. M. Carrico, S. M. Kreidenweis, A. J. Prenni, P. J. DeMott, J. L. Collett Jr., and H. Moosmuller (2009), Cloud condensation nucleation activity of biomass burning aerosol, *J. Geophys. Res.*, *114*, D22205, doi:10.1029/2009JD012353.

Salcedo, D., et al. (2006), Characterization of ambient aerosols in Mexico City during the MCMA-2003 campaign with Aerosol Mass Spectrometry: Results from the CENICA Supersite, *Atmos. Chem. Phys.*, *6*, 925–946.

Skamarock, W. C., J. B. Klemp, J. Dudhia, D. O. Gill, D. M. Barker, W. Wang, and J. G. Powers (2005), A description of the advanced research WRF version 2, *Rep.*, DTIC Document.

Stohl, A., C. Forster, A. Frank, P. Seibert, and G. Wotawa (2005), Technical note: The Lagrangian particle dispersion model FLEXPART version 6.2, *Atmos. Chem. Phys.*, *5*, 2461–2474.

Sun, J., Q. Zhang, M. R. Canagaratna, Y. Zhang, N. L. Ng, Y. Sun, J. T. Jayne, X. Zhang, X. Zhang, and D. R. Worsnop (2010), Highly time- and size-resolved characterization of submicron aerosol particles in Beijing using an Aerodyne Aerosol Mass Spectrometer, *Atmos. Environ.*, *44*(1), 131–140.

Sun, Y. L., G. Zhuang, A. Tang, Y. Wang, and Z. An (2006), Chemical characteristics of $PM_{2.5}$ and PM_{10} in haze-fog episodes in Beijing, *Environ. Sci. Technol.*, *40*(10), 3148–3155.

Sun, Y. L., et al. (2011), Characterization of the sources and processes of organic and inorganic aerosols in New York City with a high-resolution time-of-flight aerosol mass spectrometer, *Atmos. Chem. Phys.*, *11*(4), 1581–1602, doi:10.5194/acp-11-1581-2011.

Sun, Y. L., Z. Wang, H. Dong, T. Yang, J. Li, X. Pan, P. Chen, and J. T. Jayne (2012), Characterization of summer organic and inorganic aerosols in Beijing, China with an Aerosol Chemical Speciation Monitor, *Atmos. Environ.*, *51*, 250–259, doi:10.1016/j.atmosenv.2012.01.013.

Sun, Y. L., Z. Wang, P. Fu, Q. Jiang, T. Yang, J. Li, and X. Ge (2013a), The impact of relative humidity on aerosol composition and evolution processes during wintertime in Beijing, China, *Atmos. Environ.*, *77*, 927–934, doi:10.1016/j.atmosenv.2013.06.019.

Sun, Y. L., Z. F. Wang, P. Q. Fu, T. Yang, Q. Jiang, H. B. Dong, J. Li, and J. J. Jia (2013b), Aerosol composition, sources and processes during wintertime in Beijing, China, *Atmos. Chem. Phys.*, *13*(9), 4577–4592, doi:10.5194/acp-13-4577-2013.

Sun, Y. L., Q. Jiang, Z. Wang, P. Fu, J. Li, T. Yang, and Y. Yin (2014), Investigation of the sources and evolution processes of severe haze pollution in Beijing in January 2013, *J. Geophys. Res. Atmos.*, *119*, 4380–4398, doi:10.1002/2014JD021641.

Sun, Y. L., Z. F. Wang, W. Du, Q. Zhang, Q. Q. Wang, P. Q. Fu, X. L. Pan, J. Li, J. Jayne, and D. R. Worsnop (2015), Long-term real-time measurements of aerosol particle composition in Beijing, China: Seasonal variations, meteorological effects, and source analysis, *Atmos. Chem. Phys.*, *15*(17), 10,149–10,165, doi:10.5194/acp-15-10149-2015.

Ulbrich, I. M., M. R. Canagaratna, Q. Zhang, D. R. Worsnop, and J. L. Jimenez (2009), Interpretation of organic components from positive matrix factorization of aerosol mass spectrometric data, *Atmos. Chem. Phys.*, *9*(9), 2891–2918.

Vakkari, V., et al. (2014), Rapid changes in biomass burning aerosols by atmospheric oxidation, *Geophys. Res. Lett.*, *41*, 2644–2651, doi:10.1002/2014GL059396.

Xin, J., et al. (2015), The Campaign on Atmospheric Aerosol Research Network of China: CARE-China, *Bull. Am. Meteorol. Soc.*, *96*(7), 1137–1155, doi:10.1175/BAMS-D-14-00039.1.

Yan, P., J. Tang, J. Huang, J. T. Mao, X. J. Zhou, Q. Liu, Z. F. Wang, and H. G. Zhou (2008), The measurement of aerosol optical properties at a rural site in Northern China, *Atmos. Chem. Phys.*, *8*(8), 2229–2242, doi:10.5194/acp-8-2229-2008.

Yang, Y. R., et al. (2015), Characteristics and formation mechanism of continuous hazes in China: A case study during the autumn of 2014 in the North China Plain, *Atmos. Chem. Phys.*, *15*(14), 8165–8178, doi:10.5194/acp-15-8165-2015.

Zhang, F., et al. (2014), Aerosol hygroscopicity and cloud condensation nuclei activity during the AC3Exp campaign: Implications for cloud condensation nuclei parameterization, *Atmos. Chem. Phys.*, *14*(24), 13,423–13,437, doi:10.5194/acp-14-13423-2014.

Zhang, J. K., Y. Sun, Z. R. Liu, D. S. Ji, B. Hu, Q. Liu, and Y. S. Wang (2014), Characterization of submicron aerosols during a month of serious pollution in Beijing, 2013, *Atmos. Chem. Phys.*, *14*(6), 2887–2903, doi:10.5194/acp-14-2887-2014.

Zhang, Q., J. L. Jimenez, D. R. Worsnop, and M. Canagaratna (2007), A case study of urban particle acidity and its effect on secondary organic aerosol, *Environ. Sci. Technol.*, *41*, 3213–3219.

Zhang, Q., J. Jimenez, M. Canagaratna, I. Ulbrich, N. Ng, D. Worsnop, and Y. Sun (2011), Understanding atmospheric organic aerosols via factor analysis of aerosol mass spectrometry: A review, *Anal. Bioanal. Chem.*, *401*, 3045–3067, doi:10.1007/s00216-011-5355-y.

Zhang, T., M. Claeys, H. Cachier, S. Dong, W. Wang, W. Maenhaut, and X. Liu (2008), Identification and estimation of the biomass burning contribution to Beijing aerosol using levoglucosan as a molecular marker, *Atmos. Environ.*, *42*(29), 7013–7021, doi:10.1016/j.atmosenv.2008.04.050.

Zhang, Y. J., et al. (2015), Insights into characteristics, sources, and evolution of submicron aerosols during harvest seasons in the Yangtze River Delta region, China, *Atmos. Chem. Phys.*, *15*(3), 1331–1349, doi:10.5194/acp-15-1331-2015.

Zhao, X. J., P. S. Zhao, J. Xu, W. Meng, W. W. Pu, F. Dong, D. He, and Q. F. Shi (2013), Analysis of a winter regional haze event and its formation mechanism in the North China Plain, *Atmos. Chem. Phys.*, *13*(11), 5685–5696, doi:10.5194/acp-13-5685-2013.

Zheng, G. J., et al. (2015), Exploring the severe winter haze in Beijing: The impact of synoptic weather, regional transport and heterogeneous reactions, *Atmos. Chem. Phys.*, *15*(6), 2969–2983, doi:10.5194/acp-15-2969-2015.

Zheng, S., A. Pozzer, C. X. Cao, and J. Lelieveld (2015), Long-term (2001–2012) concentrations of fine particulate matter (PM2.5) and the impact on human health in Beijing, China, *Atmos. Chem. Phys.*, *10*(15), 5715–5725, doi:10.5194/acp-15-5715-2015.